TOMOGRAPHIC RECONSTRUCTIONS USING MAP ALGORITHMS - APPLICATION TO THE SPIDR MISSION

D.N. Ghosh Roy, K. Wilton, T.A. Cook, S. Chakrabarti
Center For Space Physics, Boston University, Boston, Massachusetts
J. Qi, G.T. Gullberg
E.O. Lawrence Berkeley National Laboratory, University of California, Berkeley

Abstract

The spectral image of an astronomical scene is reconstructed from noisy tomographic projections using maximum a posteriori (MAP) and filtered backprojection (FBP) algorithms. Both maximum entropy (ME) and Gibbs prior are used in the MAP reconstructions. The scene, which is a uniform background with a localized emissive source superimposed on it, is reconstructed for a broad range of source counts. The algorithms are compared regarding their ability to detect the source in the background. Detectability is defined in terms of a contrast-to-noise ratio (CNR) which is a Monte Carlo ensemble average of spatially averaged CNRs for the individual reconstructions. Overall, MAP was found to yield improved CNR relative to FBP. Moreover, as a function of the total source counts, the CNR varies distinctly different for source and background regions. This may be important in separating a weak source from the background.

I. INTRODUCTION

Tomographic reconstructions often involve recovering point-like emissive sources from noisy projections, the sources being located in a uniform background. The problem is typical of astronomical investigations in which localized, emissive astronomical sources are superimposed on an otherwise uniform sky. Spectral imaging of the sky in the extreme and far ultraviolet, as in the SPIDR (*Spectroscopy and Photometry of Intergalactic Diffuse Radiation*) mission [1], is an important application in this direction. In the conventional method, an imaging spectrograph is scanned across a telescopic image

of the sky formed on the entrance slit. However, the astronomical objects are generally weak in emission, and the conventional technique is handicapped by its narrow field of view (FOV) and exposure time since the instrument scans only a narrow portion of the sky at any time stage of data collection. In order to overcome these difficulties, a novel technique, called SPINR (*Spectrograph for Photometric Imaging with Numeric Reconstruction*) [2-3], was recently developed in order to keep the entire scene within the FOV of the instrument over the complete duration of data collection. The data collection is tomographic, and the imaging spectrograph employed for this purpose is equipped with a toroidal grating which acquires spectral data along the dispersion and spatial data along the cross-dispersion direction [4]. In SPINR, a two-dimensional detector is aimed at the sky and is rotated. At each angular position, the line integrals of a uniform, but infinite sky is formed through a fixed, finite FOV. The SPINR angular projections of the uniform sky are, therefore, not typical Radon transforms. Notwithstanding this, once the angular projection data is obtained, classical tomographic procedures can be applied to reconstructing the scene. Some preliminary reconstructions using SPINR technique appeared in [2-3,5].

Further applications of MAP [6] and FBP [7] tomographic algorithms are discussed in this paper. The MAP algorithms are used in the form of the *penalized maximum log-likelihood* (PML) with *entropy* (ME) and *Gibbs prior* [8-12], and *penalized least squares* (PLS) [13] with entropy prior. The MAP algorithms are nonlinear, statistical, and are considered to yield better noise performance than the linear FBP [14]. This is also the conclusion of this study. It has been shown [15-16] that ME is effective for sparse, point-like objects, and it enhances relative differences between weak and strong features in a distribution, although it does not necessarily imply enhancement in sensitivity. Recently, maximum entropy was applied *in the mean*, called *maxentropy on the mean* (MEM). In MEM, the standard ME functional, $\mathbf{f}$ log $\mathbf{f}$, $\mathbf{f}$ being the object density distribution, is used in determining an overall probability distribution the mean of which provides the reconstruction [17-18]. However, in this paper, ME was applied in its standard form, namely, using the ME functional directly into the reconstruction algorithm. A realistic prior must take into account the correlations between the neighboring elements of the density distribution. One such prior is Gibbs prior [11-12] which is considered here. The use of this prior leads to smoother reconstructions. The amount of the prior was varied in each of the nonlinear algorithms used.

In our numerical experiments, the model density distribution consisted of a localized emissive source in an otherwise homogeneous background. The total count (over the entire sinogram, that is, the sum over all the measurement rays) for the source was varied over a broad range so that the algorithms could be compared in their detectability on a wide range of counts. A contrast-to-noise ratio (CNR) was used as the criterion of detectability. Its definition involved Monte Carlo ensemble averaging of spatially

averaged, per simulation CNRs (see Section III for details). The ensemble averaged CNR was investigated as a function of total source count. Numerical results reported here show that, in general, the nonlinear methods lead to higher detectability compared to the linear FBP. This is especially true in low count regions which are of particular interest in astrophysical investigations.

The plan of the paper is as follows. Section II outlines the basic algorithms, and the associated iteration procedures. Methodological and computational details, results of numerical experiments, and discussions appear in Section III. Finally, a short summary in Section IV concludes the paper.

II. Reconstruction Algorithms

Consider an object with a density distribution $\mathbf{f}$. The object is discretized into a $P \times P$ matrix. Thus $\{f_i\}_{i=1}^{N}, N = P^2, f_i > 0, \forall i$, are the pixel values in the object. Let $\mathbf{H}$ denote the projection matrix. The ji-th element, H_{ji}, of $\mathbf{H}$, represents the intersection of the j-th ray with the i-th pixel in the object. From now onward, a matrix operator will be denoted by a bold-faced capital letter, and a vector quantity by a bold-faced lower-case letter. Let N_D, N_A be the number of detector bins and the number of angular projections, respectively. Then $M = N_D N_A$ is the total number of ray measurements. Let $\mathbf{g} = \{g_i\}_1^M$ represent the $M \times 1$ vector. The data in the j-th detector bin, g_j, is given by

$$g_j = \sum_{i=1}^{N} H_{ji} f_i + n_j = \overline{g}_j + n_j. \tag{1}$$

$\overline{g}_j = \sum_{i=1}^{N} H_{ji} f_i$ is the noiseless projection in the j-th ray, $\mathbf{f}$ being the given object. $\mathbf{f}$ is unknown and is to be recovered from the noisy data $\mathbf{g}$. When the data contain Poisson noise, the mean and variance, σ_j^2, of g_j both equal $\overline{g}_j$. As written in Eq. (1), the noise $\mathbf{n}$ has zero mean, and its covariance is the same as the covariance of $\mathbf{g}$.

The MAP reconstruction algorithms of PML and PLS are described in this Section. Tomography being an ill-posed problem, regularization is necessary, and this motivates the penalization. In PML, the Poisson nature of noise in the data explicitly enters into the algorithm, whereas it is indirect in PLS. Each of these algorithms are described below starting with the penalized maximum log-likelihood with entropy prior.

A. The Penalized Maximum Log-likelihood (PML) With Entropy Prior

Nonlinear, statistical methods of image reconstruction frequently use the concept that the reconstructed distribution is, in some sense, also the most probable one. The solutions by these methods involve

extremizing some joint probability distribution of the object $\mathbf{f}$ and the data $\mathbf{g}$. The distribution considered here is the conditional probability, $p(\mathbf{g}|\mathbf{f})$, or the *global likelihood* of the data $\mathbf{g}$ given the object $\mathbf{f}$. Assume that each detector bin is subjected to an independent Poisson process. Then an individual projection, g_j, in the j-th detector bin is distributed according to

$$p(g_j|\mathbf{f}) = \left[e^{-\sum_{i=1}^{N} H_{ji} f_i}\right] \frac{(\sum_{i=1}^{N} H_{ji} f_i)^{g_j}}{g_j!}. \tag{2}$$

The global likelihood $p(\mathbf{g}|\mathbf{f})$ is the product of the individual distributions in Eq. (2). Therefore,

$$p(\mathbf{g}|\mathbf{f}) = \prod_{j=1}^{M} \left[e^{-\sum_{i=1}^{N} H_{ji} f_i}\right] \frac{(\sum_{i=1}^{N} H_{ji} f_i)^{g_j}}{g_j!}. \tag{3}$$

From the computational point of view, it is convenient to work with the *log-likelihood*, $log\{p(\mathbf{g}|\mathbf{f})\}$, of $p(\mathbf{g}|\mathbf{f})$, instead of the global likelihood $p(\mathbf{g}|\mathbf{f})$ itself. Moreover, extremizing the log-likelihood is equivalent to extremizing the global likelihood. From Eq. (3), the log-likelihood is obtained as:

$$log\{p(\mathbf{g}|\mathbf{f})\} = \sum_{j=1}^{M} \left[g_j log \left\{ \sum_{i=1}^{N} H_{ji} f_i \right\} - \sum_{i=1}^{N} H_{ji} f_i - log(g_j!) \right]. \tag{4}$$

Next consider the maximization of the objective function:

$$\Phi(\mathbf{f}) = log\ \{p(\mathbf{g}|\mathbf{f})\} + \beta \Psi(\mathbf{f}). \tag{5}$$

$\Psi(\mathbf{f})$ will be represented by the *entropy functional*, namely, $\Psi(\mathbf{f}) = -\mathbf{f}\ \log\ \mathbf{f}$. β is a weighting factor which controls the smoothness of the solution. Multiplication and division of two vectors $\mathbf{a}, \mathbf{b}$, is to be considered in a pointwise sense. In other words, $\mathbf{ab} = a_i b_i$, and $\mathbf{a}/\mathbf{b} = a_i/b_i$. Differentiating Eq. (5) with respect to $\mathbf{f}$, using Eq. (4), and setting the result to zero results in the optimality condition:

$$0 = -\ \mathbf{H}^T \mathbf{\Lambda}_p^{-1} \mathbf{g} - \left[\mathbf{H}^T \mathbf{\Lambda}_p^{-1} \mathbf{H}\right] \mathbf{f} - \beta(\mathbf{1} + log\ \mathbf{f}). \tag{6}$$

In Eq. (6), $\mathbf{p} = \mathbf{Hf}$, $\mathbf{\Lambda_z}$ represents a diagonal matrix, the diagonal elements of which are the components of the vector $\mathbf{z}$, that is, $(\mathbf{\Lambda_z})_{\ell\ell} = z_\ell$. In component form, Eq. (6) is:

$$-\beta(1 + log f_\ell) + \sum_{j=1}^{M} H_{j\ell} \frac{g_j - \sum_{i=1}^{N} H_{ji} f_i}{\sum_{i=1}^{N} H_{ji} f_i} = 0, \tag{7}$$

f_ℓ being the ℓ-th component of the vector $\mathbf{f}$.

Let $s_\ell = \sum_{j=1}^{M} H_{j\ell}$ be the ℓ-th element of the vector $\mathbf{s} = \mathbf{H^T 1}$. s_ℓ represents the probability that a photon emitted from the ℓ-th element in the object will be detected by any one of the detectors. The vector $\mathbf{s}$ is known as the *sensitivity vector* [19-20]. From Eq. (7), we obtain

$$s_\ell = \sum_{j=1}^{M} H_{j\ell} \frac{g_j}{\sum_{i=1}^{N} H_{ji} f_i} - \beta(1 + log f_\ell),$$

from which

$$1 = \frac{1}{s_\ell}\left[\sum_{j=1}^{M} H_{j\ell}\frac{g_j}{\sum_{i=1}^{N} H_{ji}f_i} - \beta(1+logf_\ell)\right]. \tag{8}$$

Multiplying both sides of Eq. (8) by f_ℓ leads to the nonlinear equation $f_\ell = A(f_\ell)$, the nonlinear function $A(f_\ell)$ representing the multiplication of f_ℓ by the R.H.S. of Eq. (8). The standard method [21] for solving this equation is to cast it in an iterative format :

$$f_\ell^{(k+1)} = (1-\alpha)f_\ell^{(k)} + \alpha A(f_\ell^{(k)}). \tag{9}$$

The parameter α is introduced for the acceleration of convergence [21], and can be updated in each iteration (see Section III for details). When written fully, Eq. (9) becomes

$$f_\ell^{(k+1)} = (1-\alpha)f_\ell^{(k)} - \alpha\frac{f_\ell^{(k)}}{s_\ell^{(k)}}\left[\beta(1+logf_\ell^{(k)}) - \sum_{j=1}^{M} H_{j\ell}\frac{g_j}{\sum_{i=1}^{N} H_{ji}f_i^{(k)}}\right]. \tag{10}$$

The penalized maximum log-likelihood solution with entropy functional is obtained by iterating Eq. (10).

B. The Penalized Least Squares (PLS) With Entropy Prior

For the penalized least squares algorithm, the objective function Φ to be maximized is

$$\Phi(\mathbf{f}) = \Psi(\mathbf{f}) - \frac{\beta}{2}\left[\mathbf{Hf}-\mathbf{g}\right]^T \mathbf{\Sigma}_g^{-1}\left[\mathbf{Hf}-\mathbf{g}\right]. \tag{11}$$

In Eq. (11), $\mathbf{\Sigma}_g$ is a diagonal matrix the elements of which are given by the variance of the data $\mathbf{g}$. In other words, $\left(\mathbf{\Sigma}_g^{-1}\right)_{jj} = \sigma_j^{-2}, \sigma_j^2$ being the variance of the j-th measurement g_j. The function $\Psi(\mathbf{f})$ is, as in PML, the entropy functional. Equation (11) then gives

$$\Phi(\mathbf{f}) = -\sum_{i=1}^{N} f_i\ log\ f_i - \frac{\beta}{2}\sum_{j=1}^{M}\frac{1}{{\sigma_j}^2}\left[\sum_{i=1}^{N} H_{ji}f_i - g_j\right]^2. \tag{12}$$

The factor β is again a constant determining the smoothness of the solution.

We next differentiate Φ in Eq. (12) with respect to $\mathbf{f}$, and set the result to zero. Note that

$$\frac{1}{2}\nabla_{\mathbf{f}}|\mathbf{Hf}-\mathbf{g}|^2 = \mathbf{H}^T(\mathbf{Hf}-\mathbf{g}),$$

This yields the following compatibility condition

$$0 = \beta\mathbf{H}^T\mathbf{\Sigma}_{\mathbf{g}}^{-1}\mathbf{g} - \beta\left[\mathbf{H}^T\mathbf{\Sigma}_{\mathbf{g}}^{-1}\mathbf{Hf}\right]\mathbf{f} - (\mathbf{1}+log\ \mathbf{f}). \tag{13}$$

From Eq. (13), it follows that

$$1 = -log\ f_\ell - \beta \sum_{j=1}^{M} H_{j\ell} \frac{\sum_{i=1}^{N} H_{ji} f_i - g_j}{\sigma_j^2}. \tag{14}$$

Again as in the previous Subsection, we multiply both sides of Eq. (14) by f_ℓ, and obtain the iteration equation

$$f_\ell^{(k+1)} = (1-\alpha) f_\ell^{(k)} - \alpha f_\ell^{(k)} \left[log\ f_\ell^{(k)} + \beta \sum_{j=1}^{M} H_{j\ell} \frac{\sum_{i=1}^{N} H_{ji} f_i^{(k)} - g_j}{\sigma_j^2} \right]. \tag{15}$$

The variance, σ_j^2 is not known beforehand, but must be estimated. In an actual numerical implementation, σ_j^2 is replaced by the data, g_j, itself [3-5,22].

Equation (15) is the basic equation for the tomographic reconstruction of the unknown density distribution $\mathbf{f}$ using the penalized least squares with entropy prior.

C. The Maximum Log-likelihood With Gibbs Prior

In this subsection, we discuss the maximum log-likelihood algorithm with Gibbs prior in place of the entropy functional. Gibbs priors have been adopted as suitable priors in image reconstruction and many other applications of image processing. The Markovian properties of these distributions make them theoretically attractive as a formalism for describing empirical local image properties, as well as computationally appealing since the local nature of their associated energy functions result in computationally efficient update strategies. The prior functions can be chosen to attempt to reflect that the images are locally smooth yet can also have rather sharp transitions. Here we use a simple Gaussian model.

Let $f(j)$ be the value of $\mathbf{f}$ at the j-th pixel in the object, and $f_a(j)$ the value of the density at a pixel adjacent to the j-th pixel, but in the direction a. Thus $a = e$ refers to the pixel which is adjacent to the center pixel $f(j)$, but to the east of it, and similarly for $a = s, ne, se$ for south, northeast and southeast, respectively. Moreover, we define the discrete approximate directional derivative, $f'_a(j)$, of $\mathbf{f}$ at j in the direction a by

$$f'_a(j) = f(j) - f_a(j). \tag{16}$$

The objective function for the MAP algorithm with Gibbs prior is given by

$$\Phi(\mathbf{f}) = log\ p(\mathbf{g}|\mathbf{f}) - \beta U(\mathbf{f}). \tag{17}$$

As before, β is the weight factor which controls the amount of the prior $U(\mathbf{f})$. We consider a clique of $f(l)$ consisting of 8 nearest neighbors, and use the following Gibbs prior

$$U(f) = \sum_{j=1}^{N} [f'^2_e(j) + f'^2_s(j) + \frac{1}{\sqrt{2}}\{f'^2_{ne}(j) + f'^2_{se}(j)\}]. \tag{18}$$

Substitute Eqs. (4), (16) and (18) in (17). Upon differentiating the resulting Φ with respect to $f(l)$, and setting it to zero gives:

$$0 = \sum_{j=1}^{M} H_{jl} \frac{\sum_{j=1}^{N} H_{jl} f(l) - g_j}{\sum_{j=1}^{N} H_{jl} f(l)} + 2\beta[(f(l) - f_e(l)) + (f(l) - f_s(l)) + \frac{1}{\sqrt{2}}(f(l) - f_{ne}(l)) + \frac{1}{\sqrt{2}}(f(l) - f_{se}(l))]. \tag{19}$$

Simplifying Eq. (19) yields

$$0 = \sum_{j=1}^{M} H_{jl} \frac{\sum_{j=1}^{N} H_{jl} f(l) - g_j}{\sum_{j=1}^{N} H_{jl} f(l)} + \beta[(4 + 2\sqrt{2})f(l) - 2(f_e(l) + f_s(l)) - \sqrt{2}(f_{ne}(l) + f_{se}(l))]. \tag{20}$$

The log-posterior density function is maximized using a preconditioned gradient algorithm. The update equation is

$$\mathbf{f}^{(k+1)} = \mathbf{f}^{(k)} + \lambda \mathbf{M}^{(k)} \nabla \Phi(\mathbf{f}^{(k)}). \tag{21}$$

The preconditioner $\mathbf{M}^{(k)}$ is given by

$$\mathbf{M}^{(k)} = \Lambda^{(k)}_{\mathbf{f}/\mathbf{S}}.$$

$\nabla \Phi(\mathbf{f}^{(k)})$ is the gradient of the objective function (17) at $\mathbf{f}^{(k)}$, and is given by the RHS in Eq. (20). The parameter λ is obtained by a one-dimensional line search.

Gibbs prior can also be written as $U(\mathbf{f}) = (1/2)\mathbf{f}^T \mathbf{T} \mathbf{f}$. $\mathbf{T}$ is a block Toeplitz matrix, with diagonals equal to $4 + 4/\sqrt{(}2)$. A maximum of 8 elements in each column (or row) are nonzero next to the diagonal. They correspond to the eight neighboring pixels. The entry values are either -1 or $-1/\sqrt{2}$, depending on their locations.

III. Methods and Numerical Results

Methods

The MAP algorithms with maximum entropy in Eqs. (10) and (15), and with Gibbs prior in Eq. (21), were applied to the reconstruction of an object consisting of a uniform background (the sky) with a localized, emissive source superimposed on it. The objective is to detect the source in the presence of

the background. The measure of *detectability* is a contrast-to-noise ratio, the evaluations of contrast and noise being detailed in this section.

Let the scene be described as

$$\mathbf{f}(\mathbf{x}) = \mathbf{f}_b \chi_{R,0}(\mathbf{x}) + \mathbf{f}_f \chi_{r,\mathbf{a}}(\mathbf{x}). \tag{22}$$

$\mathbf{f}_b$ and $\mathbf{f}_f$ are constants, and subscripts b and f indicate background and foreground or source, respectively. $\chi_{d,\mathbf{c}}(\mathbf{x})$ is the characteristic function of a region of size d with center at $\mathbf{c}$. That is, $\chi_{d,\mathbf{c}}(\mathbf{x}) = 1$ if $\mathbf{x}$ is in the region, and zero otherwise. In Eq. (22), $R > r$. The point $\mathbf{a}$ is assumed to be sufficiently far from the boundary of the reconstruction region. $\chi_{R,0}(\mathbf{x}), \chi_{r,\mathbf{a}}(\mathbf{x})$ can be termed [23] the *background* and *foreground area,* respectively. The reconstructed image, $\mathbf{f}_f^{re}(\mathbf{x})$, of the foreground is of the form

$$\mathbf{f}_f^{re}(\mathbf{x}) = \phi(\mathbf{x}; \mathcal{A}, \mathbf{f}_f, \mathbf{f}_b) \chi_{r',\mathbf{a}}(\mathbf{x}; \mathcal{A}). \tag{23}$$

ϕ is a nonlinear function of the arguments, $\mathcal{A}$ denoting the algorithm used for reconstruction. $\chi_{r',\mathbf{a}}(\mathbf{x}; \mathcal{A})$ in Eq. (23) is a characteristic function of some radius r', and may be viewed as the *region-of-interest recovery function* [24], the foreground being the region of interest. Note that if $\mathcal{A}$ = filtered-backprojection, then $\mathbf{f}_f^{re}(\mathbf{x}) = \mathbf{f}_f \tilde{\chi}_{r',\mathbf{a}}(\mathbf{x}; FBP)$, where $\tilde{\chi}_{r',\mathbf{a}}(\mathbf{x}; FBP)$ is the so-called *disk image function* [24], which is the FBP reconstruction of the characteristic function $\chi_{r',\mathbf{a}}(\mathbf{x})$. The argument $\mathcal{A}$ will be dropped in $\chi_{r',\mathbf{a}}(\mathbf{x}; \mathcal{A})$ in what follows.

Assume that an estimate of the background has been obtained. Subtracting this estimated background from Eq. (23) results in the source contribution, $\mathbf{f}_s^{re}(\mathbf{x})$, to $\mathbf{f}_f^{re}(\mathbf{x})$. Integrating (see below) $\mathbf{f}_s^{re}(\mathbf{x})$ over $\chi_{r',\mathbf{a}}(\mathbf{x})$ defines the contrast C. Thus defined, C represents the total number of photons within $\chi_{r',\mathbf{a}}(\mathbf{x})$. CNR for a given reconstructed image is obtained by dividing the contrast C by an appropriate measure of the uncertainty of the restoration as discussed below. It should be mentioned that a related definition of CNR was used by Qi and Leahy [25]. However, these authors used a *contrast impulse response* for C which involved the derivative of the mean reconstruction instead of $\mathbf{f}_s^{re}(\mathbf{x})$.

The determination of contrast involves integrating $\mathbf{f}_s^{re}(\mathbf{x})$ over $\chi_{r',\mathbf{a}}(\mathbf{x})$. It is, therefore, necessary to estimate $\chi_{r',\mathbf{a}}(\mathbf{x})$. The knowledge of the point-spread-function (PSF) of the reconstruction algorithm can be used for this purpose. It should be noted that the point-spread-function in a nonlinear algorithm may not be unique, but may vary with location and intensity of the source. However, in the numerical computations of this paper, the PSF was used only as an indicator of $\chi_{r',\mathbf{a}}(\mathbf{x})$, or equivalently, the number of pixels to be summed.

The determination of the noise uncertainty is determined as follows. Given a reconstruction, the mean of its pixel values is calculated over the image except those pixels that are in the region-of-interest.

With this mean, the pixel variances are calculated, and subsequently averaged over the same area used in the calculation of the mean. The corresponding standard deviation is then considered to be the noise uncertainty. Dividing the contrast by this uncertainty, CNR is obtained.

The CNR described above is the CNR for a single reconstruction. However, direct Monte Carlo simulations were performed. The CNR that was adopted as the measure of detectability was obtained by ensemble averaging the CNRs of the individual restorations over the Monte Carlo reconstructions. Let $L,\ \tilde{n},$ denote the total number of restorations, and the number of pixels in the region-of-interest, respectively. N_R is the total number of pixels in a region of radius R. R is smaller than the radius of the boundary of the reconstruction region. Then $\tilde{N}_R = N_R - \tilde{n}$ is the number of pixels outside the region-of-interest used for sample averaging. Let $\overline{f}^{\ell}$ be the ℓ-th sample mean, that is, the mean in the ℓ-th restoration. Then $\overline{f}^{\ell} = (1/\tilde{N}_R)\sum_{n=1}^{\tilde{N}_R} f_n^{\ell}$. The ℓ-th sample variance is, therefore,

$$\sigma_{\ell}^2 = \frac{1}{\tilde{N}_R - 1}\sum_{n=1}^{\tilde{N}_R}\left(f_n^{\ell} - \overline{f}^{\ell}\right)^2, \tag{24}$$

from which the ℓ-th standard deviation is σ_{ℓ}. The ℓ-th CNR, $(CNR)^{\ell}$, follows as

$$(CNR)^{\ell} = \frac{1}{\sigma_{\ell}}\sum_{n=1}^{\tilde{n}}\left(f_n^{\ell} - \overline{f}^{\ell}\right), \tag{25}$$

and the ensemble averaged CNR, (denoted also by CNR) is

$$CNR = \frac{1}{L}\sum_{\ell=1}^{L}(CNR)^{\ell}. \tag{26}$$

On the basis of the PSF data shown in Figure 2, it was decided to sum over a 3×3 region around the target pixel. The number of pixels $\tilde{n}$ was thus 9.

As mentioned in Section IIa, the variance, $\Sigma_{\mathbf{g}},$ in the data that appears in the iteration Eq. (15) for PLS, is not known a priori, and must be estimated. In actual computations, $\Sigma_{\mathbf{g}}$ was replaced by the noisy data, $\mathbf{g},$ itself with the proviso that $\mathbf{g}$ was to be replaced by unity in the event that the mean count $\overline{\mathbf{g}}$ was nullified by the noise.

A few words are in order at this point regarding the determination of the relaxation parameter α in Eq. (9). An analytical determination of this parameter was shown by Isaacson and Keller [21] to require severe restriction *viz* that the Jacobian matrix of the nonlinear function $A(\mathbf{f})$ in Eq. (9) must be strongly diagonally dominant. However, the lack of strong diagonal dominance in the projection-backprojection matrix $\mathbf{H}^T\mathbf{H}$ along with the presence of the logarithmic terms in the reconstruction equations renders the satisfaction of such restrictive conditions highly unlikely in tomographic imaging. However, the objective functions in Eqs. (5) and (11) are strictly convex as also the domain of the solutions, namely,

$\mathbf{f} \in R^N,\ \mathbf{f} > 0, \mathbf{f}\ \log\ \ \mathbf{f} < \infty$. Under these conditions (which extend to the weaker condition $\mathbf{f} \geq 0$,) the optimization problems (10) and (15) have unique solutions [26]. In that case, as shown in [21], the iterations converge for some choice of α. We adopted the following phenomenological choice of this parameter, and our iterations converged in the stopping criterion of a steady χ^2 defined as:

$$\chi^2 = \frac{1}{N}\sum_{j=1}^{M}\frac{\sum_{i=1}^{N}\left[H_{ji}f_i - g_j\right]^2}{g_j}.$$

An inspection of Eq. (10) and Eq. (15) shows that during the initial stages of iteration, α must not be too small, whereas as the iterations proceed, its value must gradually diminish. We, therefore, started with a high value of α, such as $\alpha = 100$. As the iterations proceeded, α was slowly increased until χ^2 stopped decreasing. At that point, α was reduced by an order of magnitude, and the procedure was repeated until convergence in which stage the value of α could be as small as 10^{-9}. In the case that $\mathbf{f}$ becomes negative, the last iteration is rejected and the calculation is moved to the next level of α.

Finally, it should be mentioned that reconstructions were also performed for FBP with Ram-Lak filter [7]. The discrete FBP equation is:

$$f(m,n) = \frac{1}{N_A}\sum_{i=1}^{N_A}\sum_{k=0}^{K-1} g_{i,t(m,n)+k}h_k.$$

$t(m,n)$ is the bin index of pixel (m,n), and the Ram-Lak filter is given by:

$$\mathbf{h} = \{\cdots, -9\pi^{-2}, 0, -\pi^{-2}, 0.25, -\pi^{-2}, 0, -9\pi^{-2}, \cdots\}.$$

The integer K was 11 in our case.

Numerical Results

Numerical calculations were carried out under the following conditions. The conditions described are for the specific design of SPIDR. The object size was 64×64, and the number of detector bins and the number of angular projections (over 0 to π) were both 64. Thus $N_D = N_A = 64$. The projection matrix $\mathbf{H}$ was obtained as follows. In SPINR, the 2D detector rotates around its center. The area of reconstruction is, therefore, a circle of diameter $\sqrt{2}N_D$. Thus for a 64×64 object, the circle encompasses roughly 90 pixels on its diameter. The sinogram for an arbitrary pixel within and on the circle is determined numerically, that is, without using the analytical Radon transform. The entire $\mathbf{H}$ matrix is subsequently obtained by sequentially scanning across the circular domain beginning with the lowermost left pixel. All computations, including the generation of the data, were performed with the projection (and backprojection) matrix thus generated. The total count (i.e., count over the entire

sinogram) for a background pixel was 11, and the number for the source was varied, ranging from 20 to 7500. These are reasonable numbers for an astronomical scene. Poisson noise was added to the data, and 200 Monte Carlo reconstructions were performed. $\sigma_\ell^2,\ (CNR)^\ell$, and CNR, were obtained as described above according to Eqs. (24)-(26).

Some typical examples of PSFs are shown in Figures 1 and 2. Figure 1 shows log displays of some reconstructed PSF images, whereas the photon collection characteristics of the algorithms are illustrated in Figure 2. The vertical axis in Figure 2 represents the percentage of the signal, that is, the total number of photons in the annuli, each one pixel thick, and of increasing radii from the center or the source pixel. The plots of Figure 2, therefore, indicate how tightly the source emission is swept up by different algorithms. As can be seen from this figure, the nonlinear methods collect photons more tightly than the linear FBP. This is evidenced by the faster fall-off of PML and PLS curves 1-6 compared to the FBP curve 7 which meanders without tapering off with increasing radius.

A few examples of typical reconstructions are shown in Figures 3 and 4. The images are self-explanatory. The reconstructions shown in Figure 3 are some typical members of the Monte Carlo ensemble, and correspond to S = 200. Some typical mean reconstructed images are displayed in Figure 4 for S = 100. FBP images with Ram-Lak filter are also shown in these figures.

The Monte Carlo ensemble averaged contrast-to-noise ratio, is plotted in Figures 5a and 5b as functions of total source count S. Figure 5a contains results for PML and PLS with entropy prior, FBP and the background. Figure 5b is the same as Figure 5a, but for Gibbs prior. The horizontal line in the figures is the 3σ detection line, whereas the straight line, marked A, corresponds to the *exact* reconstruction. An exact reconstruction is the one where the uncertainty in the data equals the uncertainty in the reconstructed image, and in which the density distribution is restored perfectly. Let $\sigma^{re},\ \sigma_g$, denote the uncertainty in the restoration and data, respectively. Then, in general, $\sigma^{re} = \kappa(\mathbf{f})\sigma_g$. The factor κ, which depends upon $\mathbf{f}$, accounts for the intervening reconstruction algorithm. In an exact reconstruction, $\kappa = 1,\ \kappa$ being > 1 otherwise. In the present case, with the total background count of 11, and Poisson noise in the data, $\sigma^{re} = \sqrt{11}$ for the exact reconstruction. Therefore, $(CNR)_{exact} = C_{exact}/\sqrt{11}$. The line A represents $(CNR)_{exact}$. In Figure 5b, two sets of results are shown for Gibbs prior. The data corresponding to Method 2 in the inset were obtained by the procedures described in the previous section, that is, summing over the 3×3 region. The data for Method 1 were obtained as follows (see Discussions below). In Method 1, the statistics of the background were determined over a 30×30 region, but excluding a 13×13 region, both around the source pixel. The contrast was still determined by summing over 3×3 pixels.

The CNR data for a background point away from the source are also plotted in Figure 5, and are

indicated by stars. For the sake of the clarity of presentation, data are displayed only for a single pixel, but for the various algorithms shown in the legend. In Figure 5a, the background data refer to PML, PLS and FBP, whereas in Figure 5b, the results are for PML with Gibbs prior and FBP. In both Figure 5a and 5b, multiple points correspond to a single fixed S. Their occurrences are due to the different algorithms used. Moreover, the background data points which are missing in the plots fall outside the scale of the figures. Also, the absolute values of the background CNR are plotted here. The results for an arbitrary background pixel away from the region-of-interest show similar behavior.

Finally, a typical behavior of the relaxation parameter α as a function of iteration is displayed in Figure 6.

Discussions

The PSFs shown in Figures 1 and 2 correspond to a single source point without the background. Consequently, PSFs in these figures are not directly related to those, for example, in Figures 3 and 4. As pointed out above, the only use of the PSFs was to obtain an estimate of the region-of-interest. Moreover, since the object to be recovered is unknown, this is the PSF which can be directly obtained in practice.

The reason for two sets of data in Figure 5b for Gibbs prior is as follows. Note that the trend of CNR vs. β in Method 2 undergoes a reversal at S = 7500. This is a consequence of the PSF for this algorithm being sufficiently wide at this count (Figure 2) so that much of the energy falls outside the summed area. It has been shown [27] that the PSF in MAP reconstructions are wider in high count regions than in low count regions. Since the signal is strong, excluding only 3×3 pixels is not sufficient. CNR was recalculated by determining the statistics over a 30×30 region, as in Method 1, but now excluding a 13×13 region, both around the source pixel. The contrast was still determined by summing over 3×3 pixels. It is seen that the reversal of the trend at S = 7500 is eliminated.

The results of Figure 5 show that, overall, the nonlinear algorithms display increased detectability compared to FBP with Ram-Lak over a broad range of counts. PML with entropy prior and Gibbs are seen to perform particularly well, especially in low count regions. Now the detectability depends upon the region-of-interest. If this region is so chosen as to incorporate the widest PSF (of the algorithms one would choose to use), then the CNR would be determined primarily by the noise uncertainty. In that case, FBP with filters having roll-offs smoother than Ram-Lak may yield higher values for CNR compared to Ram-Lak. However, CNR being an indicator of detectability only, image resolution is to be considered simultaneously. Hence in using linear methods, both of these must be considered simultaneously. In

addition, from the point of view of comparing the merits of different methods in regard to detectability, the region-of-interest may not be allowed to accommodate the widest PSF. In that case, Ram-Lak would be the choice for linear reconstructions.

As a function of total source counts, CNR for the source behaves distinctly differently from the background regions as is evident from the data in Figure 5. The background shows no definite pattern, consisting of randomly scattered points which are mostly below the 3σ detection line. In applications in which the detection of a weak source in a background is of primary interest, as in the SPIDR mission, the existence of a distinctive trend in the source CNR compared to random background points may be important when separating a weak source from the background is an important consideration.

IV. Conclusions

In summary, an astronomical object consisting of the infinite sky with a single emissive source in the field of view was tomographically reconstructed by applying nonlinear maximum a posteriori or MAP algorithms, and the linear FBP with Ram-Lak filter. The MAP reconstruction methods included penalized maximum log-likelihood with entropy and Gibbs prior, and penalized least squares with entropy functional. Compared with FBP, the nonlinear algorithms resulted in tighter photon collection characteristics, the number of photons collected only in the source pixel itself being several times greater than in FBP. A Monte Carlo ensemble average of spatially averaged contrast-to-noise ratio was defined as the measure of detectability of the source in the presence of background. The behavior of the CNR so defined with the total count S in the source sinogram was investigated, and compared with the results of FBP. The nonlinear algorithms yielded overall higher CNR over a broad range of S, PML with entropy and Gibbs prior performing particularly well in regions of low counts. For PML, the enhancement was as high as four times. Furthermore, the behavior of CNR for a source pixel is distinctly different from that of the background. The source CNR increases with S as opposed to a totally random variation for the background. In applications in which the detection of the source is of prime interest, this constitutes an important consideration.

Acknowledgement

Funding for D.N. Ghosh Roy, K. Wilton, T. Cook and S. Chakrabarti was provided by NASA under contract NAS 5-0313 and grant NAG5-690. J. Qi and G.T. Gullberg were supported in part by the Director, Office of Science, Office of Biological and Environmental Research, Medical Sciences Division

of the U.S. Department of Energy under contract DE-AC03-76SF00098.

References

[1]. S. Chakrabarti, M. W. Bautz, C. R. Canizares, R. Cen, T. A. Cook, N. Craig, A. Dalgarno, C. Heiles, E. B. Jenkins, J. S. Lapington, H. R. Miller, J. P. Ostriker, K. R. Sembach, J. M. Shull, and A. N. Witt, "Spectroscopy and photometry of IGM's diffuse radiations (SPIDR): a proposed mission for NASA's small explorer mission," *Proc. SPIE*, vol. 4854, pp. 356, 2002.

[2]. T.C. Cook, V.J. Gsell, J. Golub and S. Chakrabarti, "SPINR - a wide-field ultraviolet spectral imaging system," *Astroph. J.*, vol. 585, pp. 1177-1190, 2003.

[3]. Y. Betremieux, T. A. Cook, D.M. Cotton and S. Chakrabarti: "SPINR, two - dimensional spectral imaging through tomographic reconstruction," *Optic. Eng.*, vol. 32, pp. 3133-3138, 1993.

[4]. D.M. Cotton, A. Stephan, T. Cook, J. Vickers, V. Taylor and S. Chakrabarti, "Tomographic extreme-ultraviolet spectrographs: TESS," *Appl. Opt.*, vol. 39, pp. 3991-3999, 2000.

[5]. T.A. Cook, A. Stephan, Y. Betremieux, D. Cotton and S. Chakrabarti, "Ultraviolet imaging spectroscopy of dust in the interstellar medium," *SPIE*, vol. 2480, pp. 105-112, 1995.

[6]. E. Levitan and G.T. Herman, "A maximum *a posteriori* probability expectation maximization algorithm for image reconstruction in emission tomography," *IEEE Trans. Med. Imag.*, vol. MI-6, pp. 185-192, 1987.

[7]. F. Natterer, *The Mathematics of Computerized Tomography*, New York, Wiley, 1986.

[8]. J.A. Fessler and A.O.Hero, "Penalized maximum-likelihood image reconstruction using space-alternating generalized EM algorithms," *IEEE Trans. Imag. Proc.*, vol. 4, pp. 1417-1429, 1995.

[9]. C. Bouman and K. Sauer, "A unified approach to statistical tomography using coordinate descent optimization," *IEEE Trans. Imag. Proc*, vol. 5, pp. 480-492, 1996.

[10]. E. Mumcuoglu, R. Leahy, S. Cherry and Z. Zhou, "Fast gradient-based methods for Bayesian reconstruction of transmission and emission PET images," *IEEE Trans. Med. Imag.*, vol. 13, pp. 687-701, 1994.

[11] R.M. Leahy and J. Qi, "Statistical approaches in quantitative positron emission tomography," *Statistics and Computing*, vol. 10, pp. 147-165, 2000.

[12] S. Geman and D. Geman, "Stochastic relaxation, Gibbs distributions, and the Bayesian restoration of images," PAMI, vol. PAMI-6, pp. 721-741, 1984.

[13]. J.A. Fessler, "Penalized weighed least-squares image reconstruction for PET," *IEEE Trans. Med.*

Imag., vol. 13, pp. 290-300, 1994.

[14] D.J. Kadrmas, "Statistically regulated and adaptive EM reconstruction for emission computed tomography," *IEEE Trans. Nucl. Sci.*, vol. 48, pp. 790-2001.

[15]. D.L. Donoho, I.M. Johnstone, A.S. Stern and J.C. Hoch, "Does the maximum entropy method improve sensitivity?," *Proc. Natl. Acad. Sci. USA*, vol. 87, pp. 5066-5068, 1990.

[16]. D.L. Donoho, I.M. Johnstone, J.C. Hoch and A.S. Stern, "Maximum entropy and the nearly black object," J.R. Stat. Soc. B, vol. 54, 41-81, 1992.

[17]. H. Gzyl and Y. Velazquez, "Reconstructions of transition probabilities by maximum entropy in the mean," pp. 192-204, in *Bayesian Inference and Maximum Entropy Methods in Science and Engineering*, Edited by R.L. Fry, 2001.

[18] P. Maréchal and A. Lannes, "Unification of some deterministic and probabilistic methods for the solution of linear inverse problems via the principle of maximum entropy on the mean," *Inverse problems*, vol. 13, pp. 135-151, 1998.

[19]. H.H. Barrett, D.W. Wilson and B.M. Tsui, "Noise properties of the EM algorithm: I. Theory," *Phys. Med. Biol.*, vol. 39, pp. 833-846, 1994.

[20]. W. Wang and G. Gindi, "Noise analysis of MAP-EM algorithms for ECT," *Phys. Med. Biol.*, vol. 42, pp. 2215- 2232, 1997.

[21]. H.B. Keller and E. Isaacson, *Analysis of Numerical Methods*, New York, Wiley, Chapter 3, pp. 120-122, 1966.

[22] D.J. Kadrmas, E.V.R. Di Bella, R.H. Huesman, G.T. Gullberg, "Analytical propagation of errors in dynamic SPECT: Estimators, degrading factors, bias, and noise". *Phys. Med. Biol.*, vol. 44, pp. 1997-2014, 1999.

[23]. B.R. Frieden and D.C. Wells, "Restoring with maximum entropy. III. Poisson sources and backgrounds," *J. Opt. Soc. Am.*, vol. 68, pp. 93-103, 1978.

[24]. D.A. Popov, E.B. Sokolova and D.V. Sushko, "Mathematical models in two - dimensional Radon tomography in Applied Problems of Radon Transform," in *Applied Problems of Radon Transform*, edited by S.G. Gindikin, American Mathematical Society, Providence, R.I., pp. 129-205, 1992.

[25]. J. Qi and R.M. Leahy, "A theoretical study of the contrast recovery and variance of MAP reconstructions from PET data," *IEEE Trans. Med. Imag.*, vol. 18, pp. 293-305, 1999.

[26]. H.W. Engl and G. Landl, "Convergence rates for maximum entropy regularization," *SIAM J. Numer. Anal.*, vol. 30, pp. 1509-1536, 1993.

[27]. J.A. Fessler and W. L. Rogers, "Spatial resolution properties of penalized-likelihood image

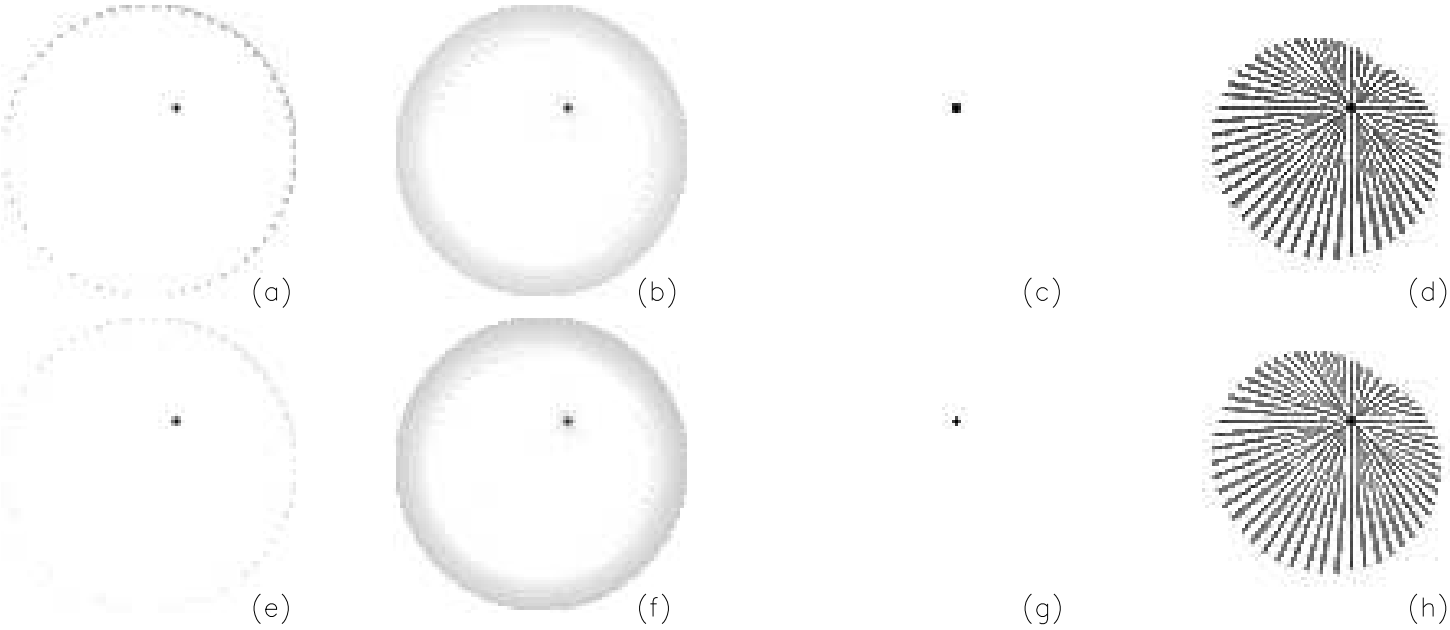

Fig. 1. Log displays of some reconstructed images of a point source. The source is off-centered at (40,45) in a 64 $\times$ 64 object. (a) PML with entropy prior, Eq. (10). (b) PLS with entropy prior, Eq. (15). (c) PML with Gibbs prior, Eq. (21). (d) FBP with Ram-Lak. The total source count S = 500 in (a)- (d). (e)-(h): Same as (a)-(d), but S = 100. Total counts refer to counts over an entire sinogram. $\beta = 1$ for all the images shown.

reconstruction: space- invariant tomographs," *IEEE. Trans. Imag. Proc.*, vol. 15, pp. 1346-1357, 1996.

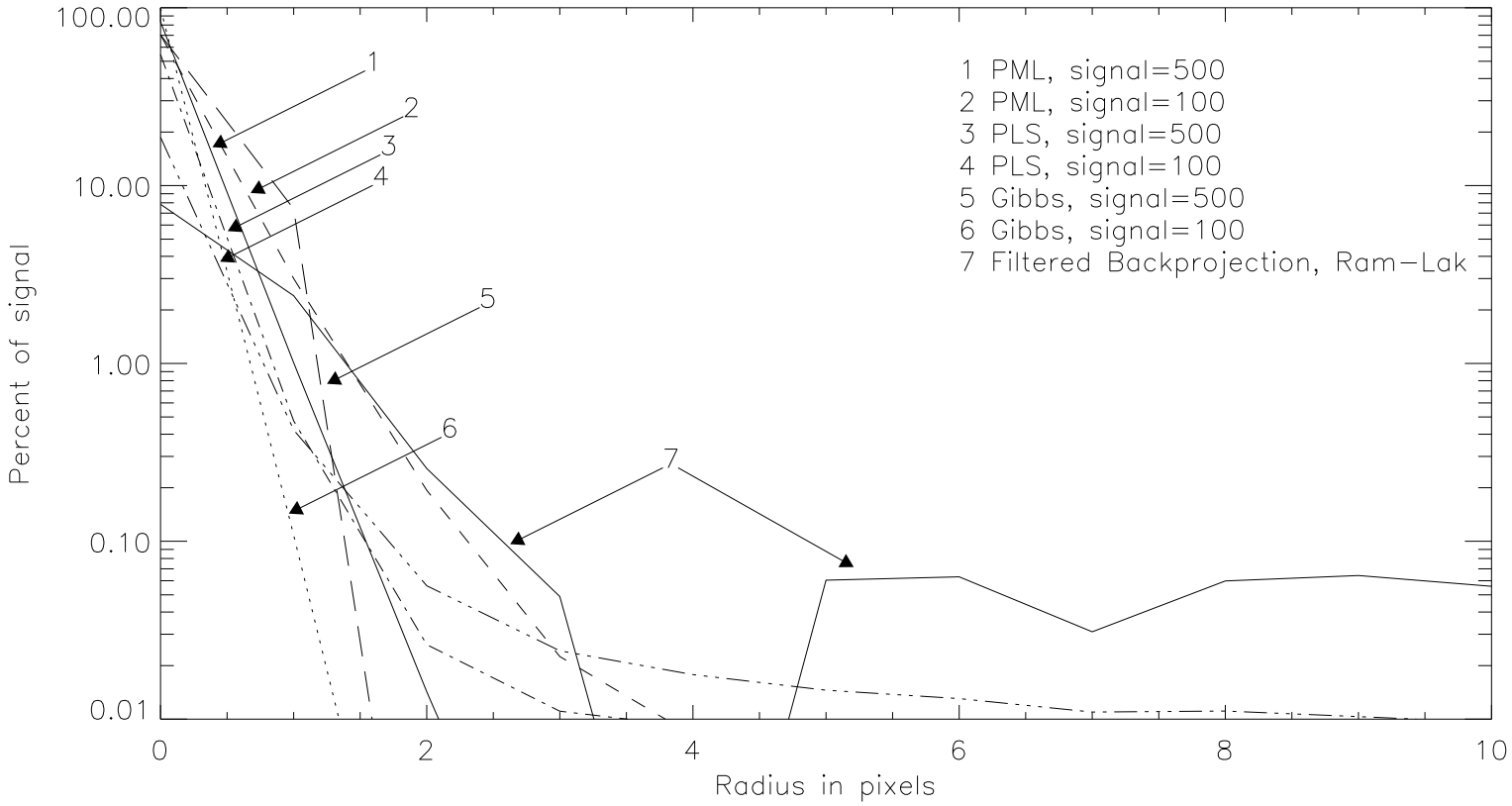

Fig. 2. Illustrations of PSFs in terms of their photon collection characteristics. The vertical axis represents the percentage of signal (total number of photons) in the annuli (each unit pixel thick), at increasing radii from the center (source) pixel. In the display, $\beta = 1$ for all the algorithms except FBP. The FBP with Ram-Lak (curve 7) clearly evidences increased diffusion relative to curves 1-6 for the nonlinear algorithms.

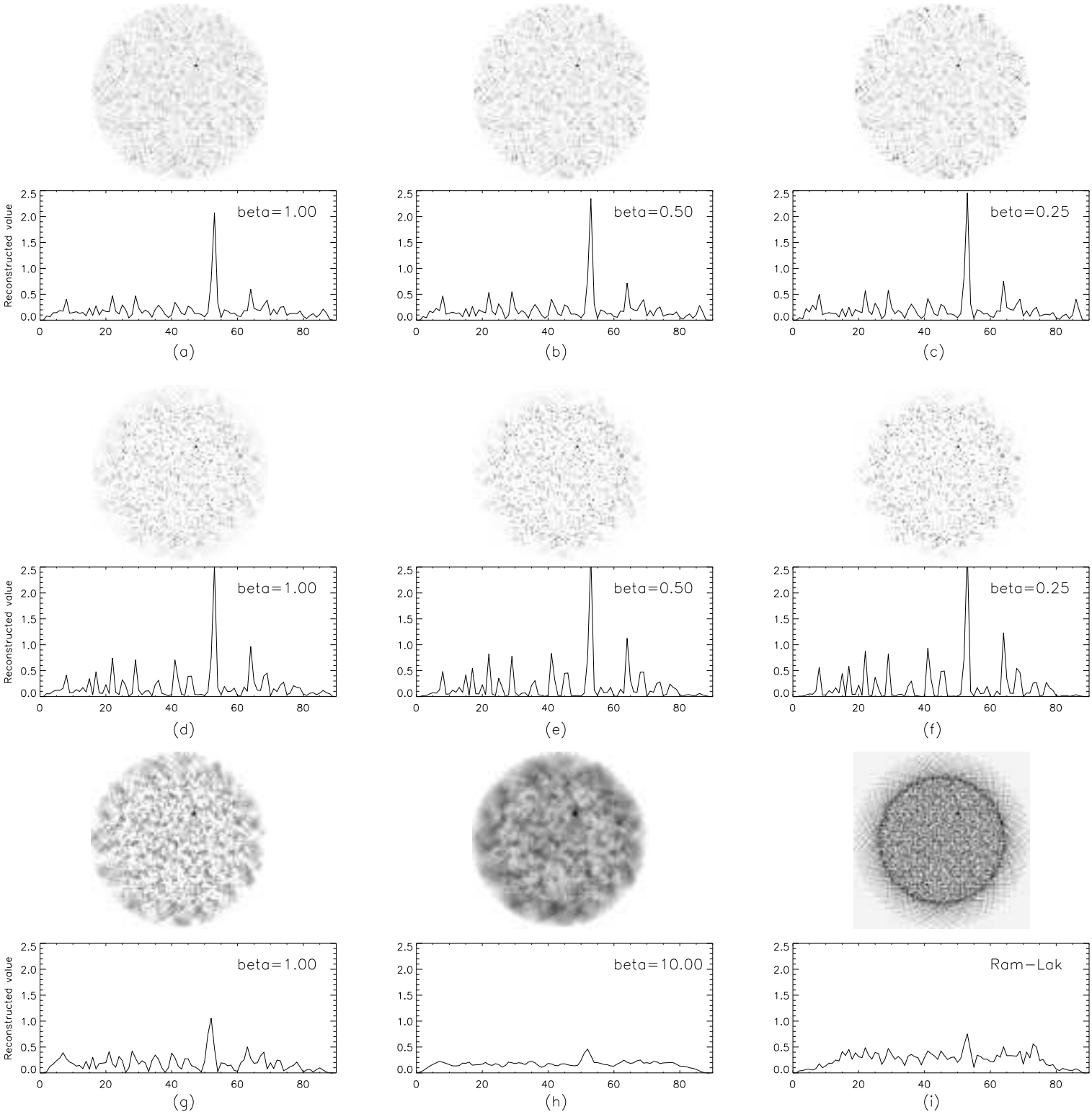

Fig. 3. Some typical reconstructions of a localized source (location is as in Figure 1) in a uniform background. Total counts for background = 11, and the displays are for the source count of 200. (a)-(c) PML with entropy prior, Eq. (10). (d)-(f) PLS with entropy prior, Eq. (15). (g)-(h) PML with Gibbs prior. (i) FBP with Ram-Lak. β values are indicated in the figures. The displays are random samples from the Monte Carlo ensemble.

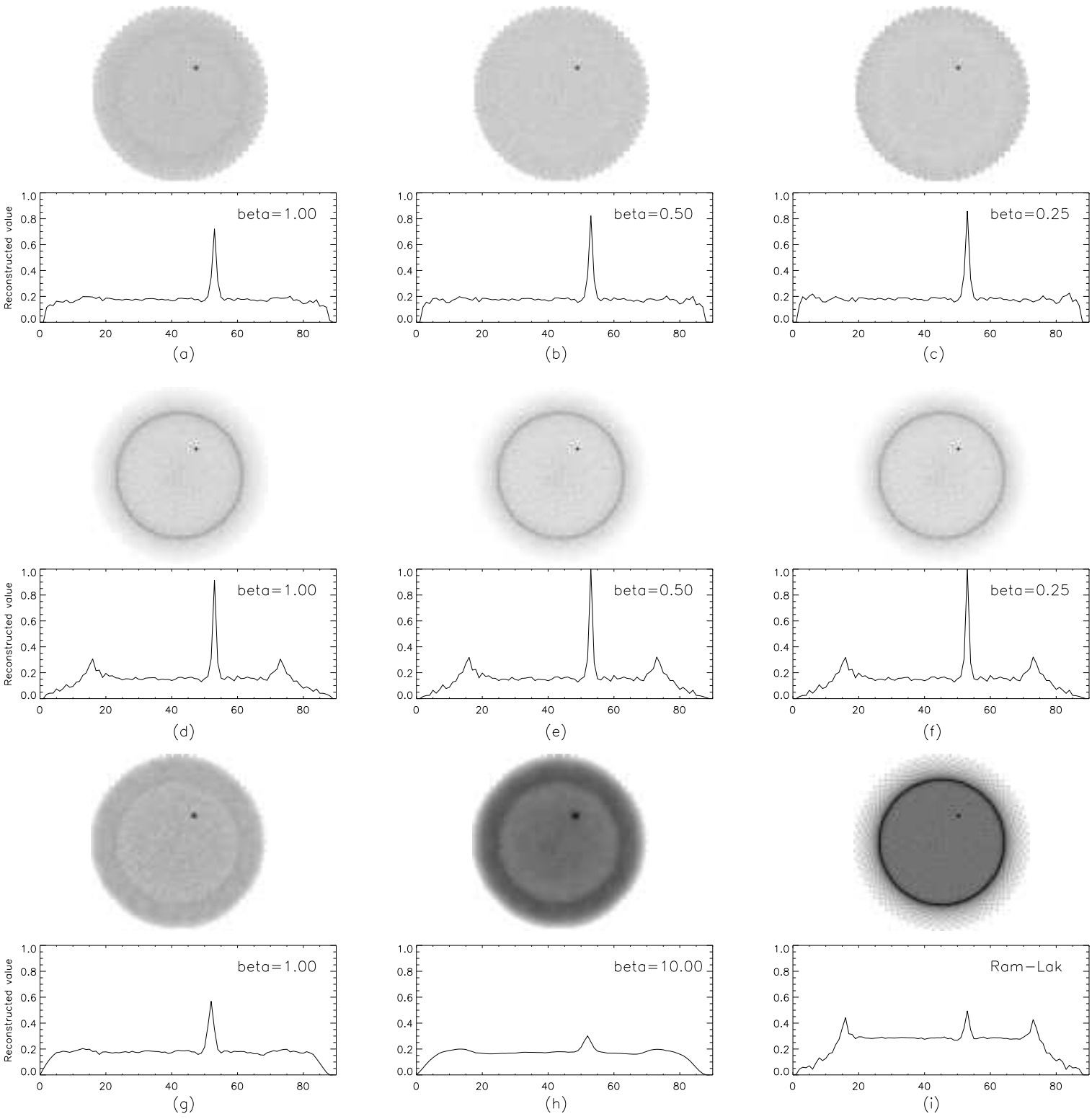

Fig. 4. Some typical mean reconstructions of a localized source (location is as in Figure 1) in a uniform background. Total counts for background = 11, and the displays are for the total source count of 100. (a)-(c) PML with entropy prior, Eq. (10). (d)-(f) PLS with entropy prior, Eq. (15). (g)-(h) PML with Gibbs prior. (i) FBP with Ram-Lak. β values are given in the figures.

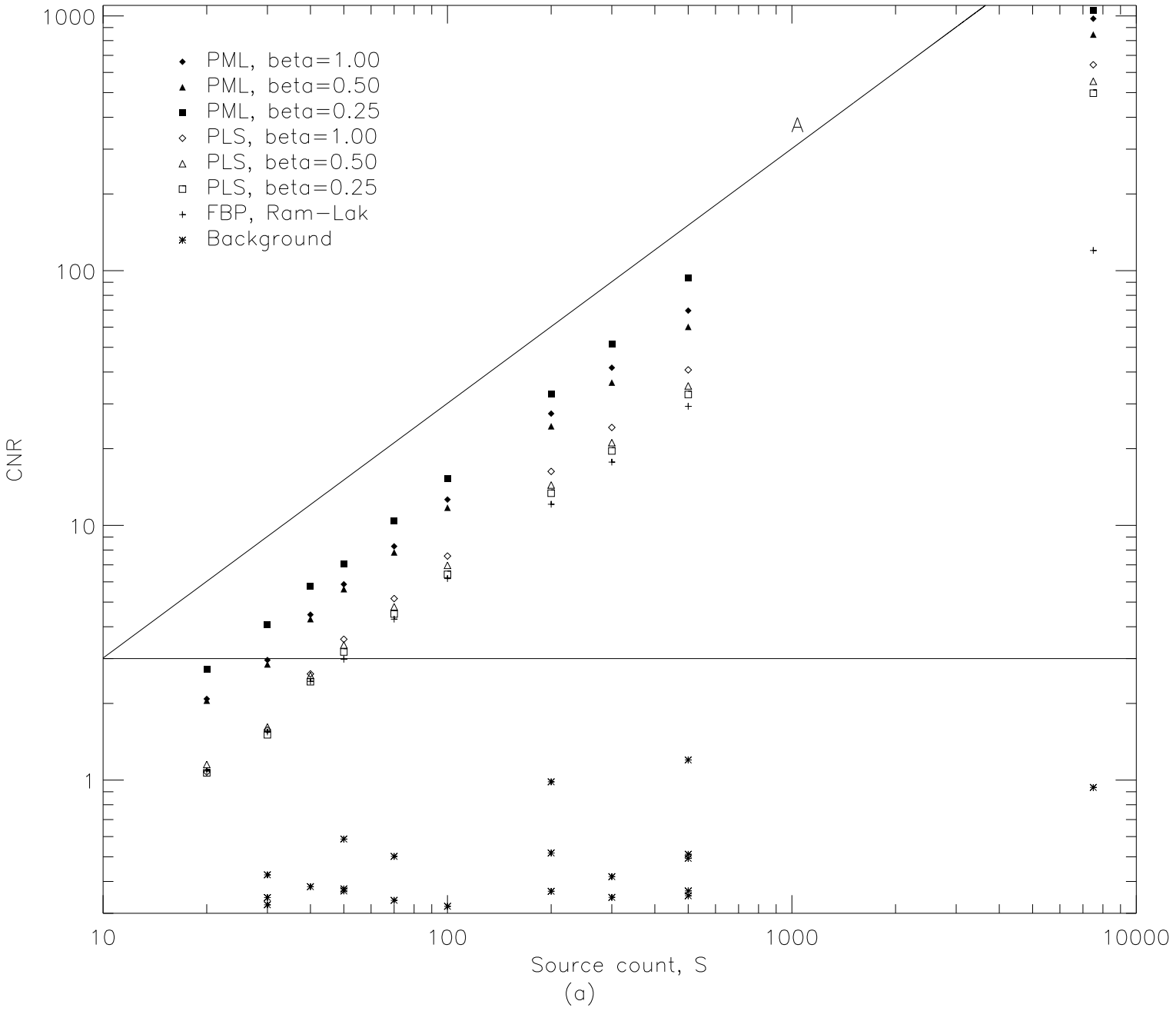

Fig. 5. (a) Illustrations of detectability for various algorithms. The Monte Carlo ensemble averaged CNR (see text) is plotted against the total source count S. Results shown are for PML with entropy prior, Eq. (10), PLS with entropy prior, Eq. (15), and FBP with Ram-Lak. Data for a single background pixel away from the source point are indicated by stars. The straight line A represents an exact reconstruction (see text), and the horizontal line corresponds to 3σ detection.

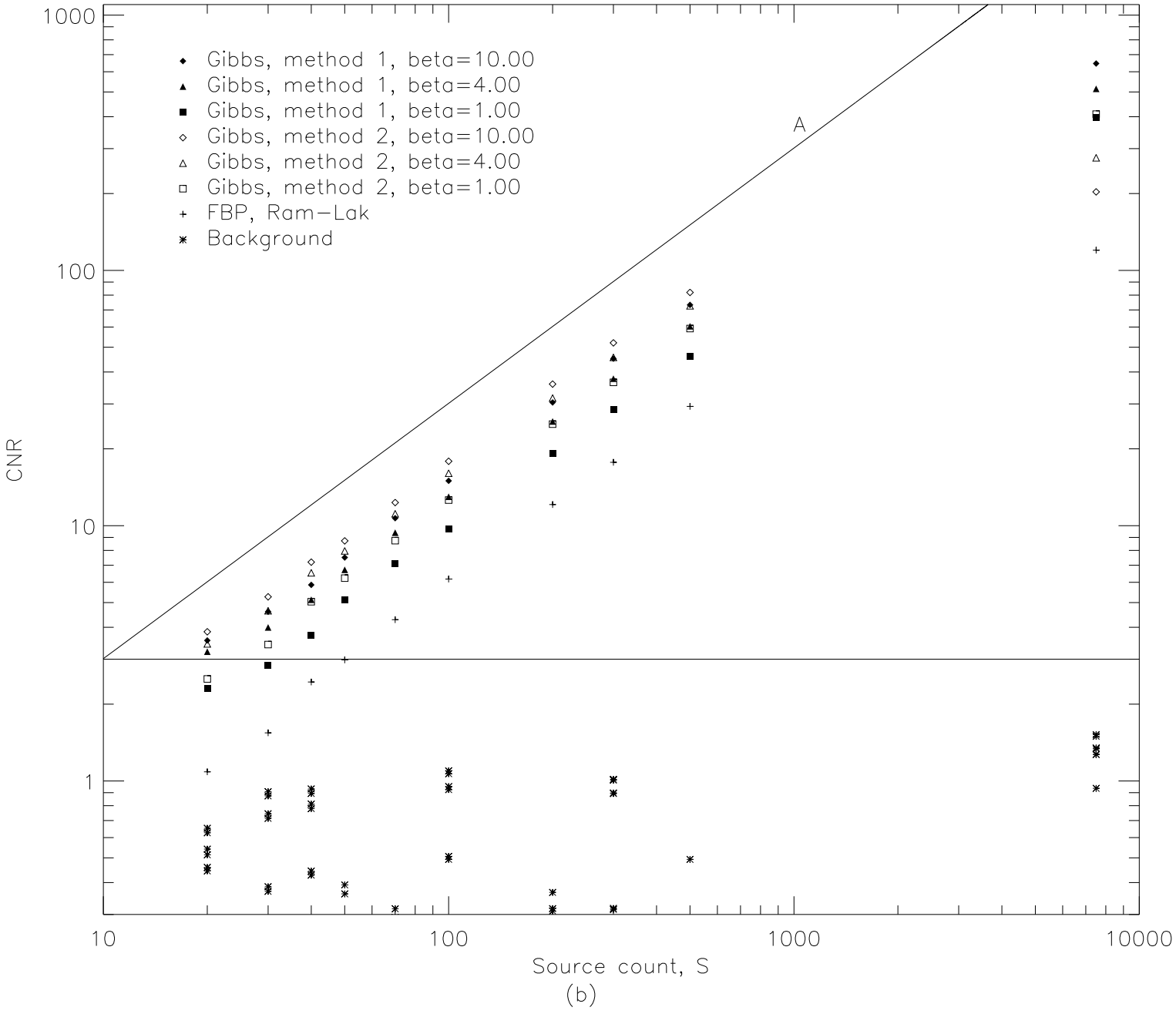

Fig. 5. (b) Illustrations of detectability for various algorithms. The Monte Carlo ensemble averaged CNR (see text) is plotted against the total source count S. Data shown are for PML with Gibbs prior. Note that two sets of data are displayed in this figure (see text). The rest is same as in Figure 5(a).

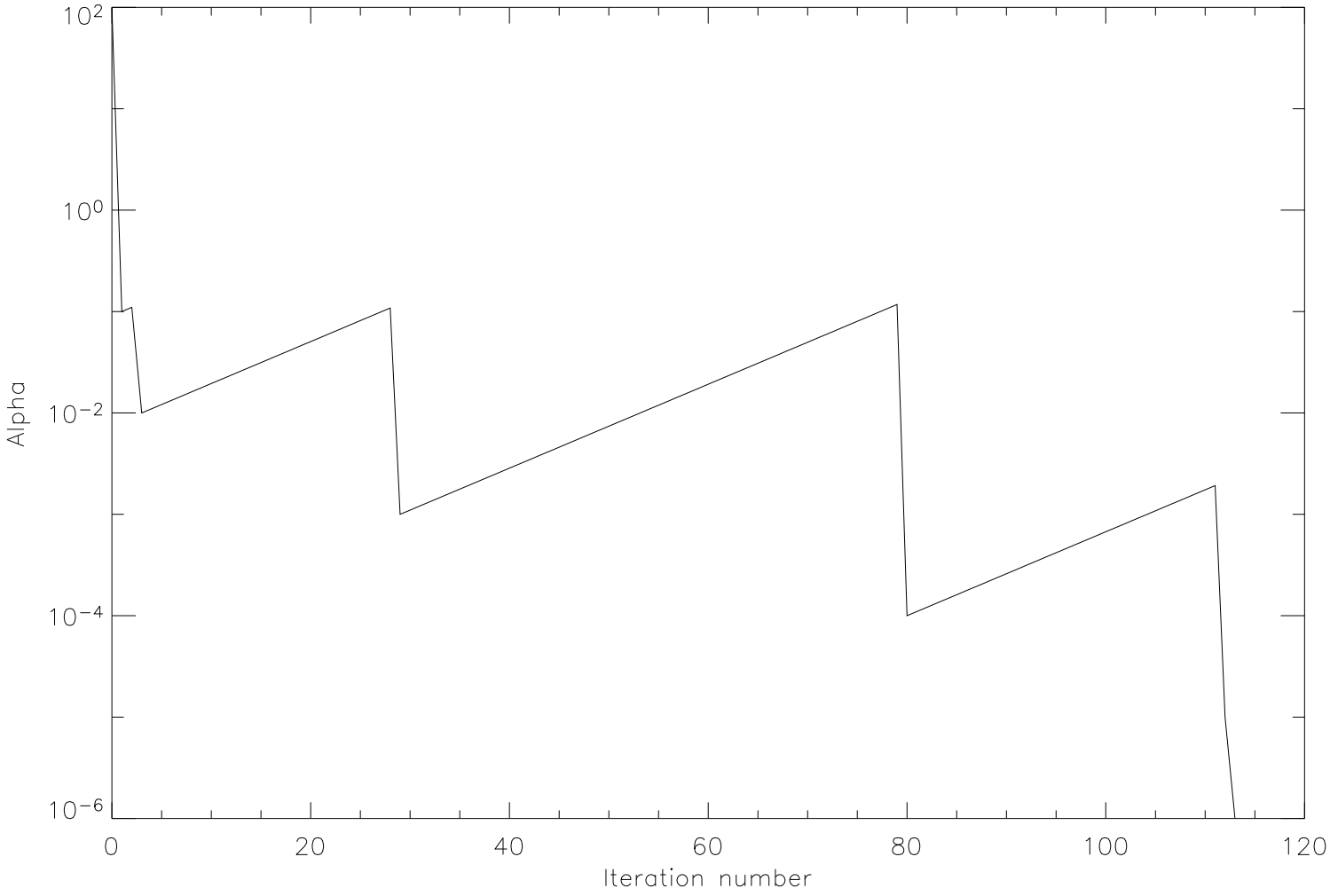

Fig. 6. A typical behavior of the phenomenological relaxation parameter α (Eq. 9). The iterations spend more time in the lower range of α as expected.